Exploiting Satellite Motion in ARAIM: Measurement Error Model Refinement Using Experimental Data

Mathieu Joerger[*] and Boris Pervan[**]
[*]*The University of Arizona, Tucson, AZ*
[**]*Illinois Institute of Technology, Chicago, IL*

BIOGRAPHIES

Dr. Mathieu Joerger obtained a Master in Mechatronics from the National Institute of Applied Sciences in Strasbourg, France, in 2002, and a M.S. and a Ph.D. in Mechanical and Aerospace Engineering from the Illinois Institute of Technology (IIT), in 2002 and 2009 respectively. He is the 2009 recipient of the Institute of Navigation (ION) Bradford Parkinson award, and the 2014 recipient of the ION Early Achievement Award. He is currently a research assistant professor at IIT, working on multi-sensor integration, on sequential fault-detection for multi-constellation navigation systems, and on safety of sense and avoid for unmanned aircraft systems.

Dr. Boris Pervan is a Professor of Mechanical and Aerospace Engineering at IIT, where he conducts research on advanced navigation systems. Prior to joining the faculty at IIT, he was a spacecraft mission analyst at Hughes Aircraft Company (now Boeing) and a postdoctoral research associate at Stanford University. Prof. Pervan received his B.S. from the University of Notre Dame, M.S. from the California Institute of Technology, and Ph.D. from Stanford University. He is an Associate Fellow of the AIAA, a Fellow of the Institute of Navigation (ION), and Editor-in-Chief of the ION journal NAVIGATION. He was the recipient of the IIT Sigma Xi Excellence in University Research Award (2011, 2002), Ralph Barnett Mechanical and Aerospace Dept. Outstanding Teaching Award (2009, 2002), Mechanical and Aerospace Dept. Excellence in Research Award (2007), University Excellence in Teaching Award (2005), IEEE Aerospace and Electronic Systems Society M. Barry Carlton Award (1999), RTCA William E. Jackson Award (1996), Guggenheim Fellowship (Caltech 1987), and Albert J. Zahm Prize in Aeronautics (Notre Dame 1986).

ABSTRACT

In this work, a new time-sequential positioning and fault detection method is derived and analyzed for dual-frequency, multi-constellation Advanced Receiver Autonomous Integrity Monitoring (ARAIM). Unlike conventional 'snapshot' ARAIM, the sequential approach exploits changes in satellite geometry at the cost of slightly higher computation and memory loads. From the perspective of users on earth, the motion of any given GNSS satellite is small over short time intervals. But, the *accumulated* effect geometry variations of redundant satellites from multiple GNSS constellations can be substantial. This paper quantifies the potential performance benefit brought by satellite motion to ARAIM. It specifically addresses the following research challenges: (a) defining and experimentally validating raw GNSS code and carrier error models over time, consistent with established ARAIM assumptions, (b) designing estimators and fault-detectors capable of exploiting satellite motion for positioning, carrier phase cycle ambiguity estimation, and integrity evaluation, and (c) formulating these processes in a computationally-efficient implementation. A modular algorithm is designed, only requiring a minor augmentation of the snapshot airborne ARAIM multiple hypothesis solution separation (MHSS) algorithm. Other modifications to enable time-sequential ARAIM include additional ground segment performance commitments, and the inclusion of extra parameters in the broadcast integrity support message (ISM). Availability is analyzed worldwide for aircraft precision approach navigation applications. Results show substantial performance improvements for sequential ARAIM over snapshot ARAIM, not only to achieve 'localizer precision vertical' (LPV) requirements using depleted GPS and Galileo constellations, but also to fulfill much more stringent requirements including a ten-meter vertical alert limit.

INTRODUCTION

This paper describes the design, analysis, and evaluation of a new time-sequential positioning and fault detection method for Advanced Receiver Autonomous Integrity Monitoring (ARAIM) using dual-frequency, multi-constellation Global Navigation Satellite Systems (GNSS). The new approach differs from prior work on 'snapshot' (or instantaneous) ARAIM algorithms [1-3] in that it also exploits satellite motion, which provides observability of constant measurement biases [4]. This

principle is used in this work to estimate floating (real valued) carrier phase cycle ambiguities, thereby improving navigation accuracy and integrity.

With the modernization of GPS, the full deployment of GLONASS, and the emergence of Galileo and Beidou, a greatly increased number of redundant ranging signals becomes available, which has recently drawn a renewed interest in RAIM. RAIM exploits redundant GNSS measurements to achieve self-contained fault detection at the user receiver [5, 6]. In particular, RAIM can help relax requirements on ground-based integrity monitors. For example, researchers in the European Union and in the United States are investigating ARAIM for worldwide vertical guidance of aircraft [1-3].

One of the primary tasks in ARAIM is to evaluate integrity risk, or equivalently, the protection levels (PL), which are probabilistic bounds on positioning errors. Integrity risk is the probability of undetected faults causing unacceptably large positioning errors. Multiple research efforts have recently been conducted to design optimal estimators and detectors that minimize the integrity risk in ARAIM, while meeting specified continuity and accuracy criteria [7-10]. These methods have been employed in the 'ARAIM Milestone 2 Report' [2] to identify the circumstances under which dual-frequency GPS/Galileo could satisfy LPV-200 requirements globally. The 'localizer precision vertical' (LPV) requirements are set to support vertical navigation during approach operations down to 200-foot altitude above ground. Reference [2] shows that worldwide coverage of LPV-200 is achievable using optimal 'snapshot' ARAIM algorithms for a wide range of nominal measurement error and fault parameters.

However, reference [2] also points out cases where LPV200 is not achievable using dual-frequency GPS and Galileo, for example, when the nominal constellations are even slightly depleted—e.g., by a single satellite in each. In addition, the alert limit (i.e., the limit on acceptable positioning errors, which defines hazardous situations) is 35 meters for LPV-200, which is much larger than, for example, the Category II precision approach alert limit requirement of 10 meters [11]. Thus, given that the methods used in [7-10] reach the best achievable performance, 'snapshot' ARAIM algorithms cannot provide global service better than LPV-200.

In response, this work explores the potential benefit of new integrity monitoring methods that exploit satellite motion in dual-frequency multi-constellation ARAIM.

Unlike 'snapshot' airborne ARAIM algorithms, where carrier-smoothed code (CSC) measurements from multiple satellites are combined at one instant in time, position estimates obtained, for example, from a batch

estimator (or finite-interval estimator [12]) are directly derived from time-sequences of raw measurements. The 'raw batch' is more computation and memory expensive, but it gives the means to exploit satellite motion over short time intervals. The upper bound on time interval is limited by the minimum mission duration for an ARAIM-equipped aircraft. A worst-case scenario would be a situation in which an aircraft is compelled to land just after takeoff. The duration of such a 'mission'—including taxi, takeoff, go-around, and landing—is assumed to be no shorter than 10-to-15 min.

This research builds upon prior work in [13] where a computationally-expensive 'raw batch' ARAIM algorithm was evaluated assuming preliminary error models over time. In this paper, we refine and validate these error models using experimental data, we implement a new modular design for the airborne batch ARAIM method (which was briefly introduced in [13] and is refined here), and we discuss the need for additional ARAIM ground segment commitments and broadcast parameters in the Integrity Support Message (ISM).

In the next section of this paper, previous research efforts are reviewed, which specifically use geometric diversity for carrier phase-based positioning. These prior references have in common that they rely on large changes in geometry from a small number of ranging sources. Conversely, in this paper, we exploit the combination of small angular variations from many space vehicles (SV). To reinforce this point, we derive an analytical expression of the positioning error variance for an illustrative aircraft navigation example using a time-sequence of carrier measurements. The positioning error variance is shown to be inversely proportional to the accumulated angular variations from visible SVs, and therefore decreases as the amount of geometry change summed over redundant satellites from multiple GNSS increases.

The third section of this paper addresses the key challenge of measurement error modeling over time. The ARAIM error models in [1-3] provide values of the instantaneous CSC measurement error standard deviations due to satellite clock and orbit ephemeris, troposphere, multipath and receiver noise. For each of these error sources, references [13, 14] describe parametric models of the time-correlation affecting raw code and carrier measurements. In this paper, we validate these error models over time using experimental data. To achieve this, GPS SV clock and orbit ephemeris errors are computed over a 10-month period by comparing broadcast ephemeris (available on the Crustal Dynamics Data Information System website) to precise orbit and clock data from the National Geospatial-Intelligence Agency (NGA), which is considered truth data. Error distributions are established to determine realistically

achievable values of the User Range Accuracy (URA) and User Range Rate Accuracy (URRA), which are key to integrity risk evaluation. URA and URRA are bounds on the satellite clock and orbit ephemeris errors, and on the rate of change of these errors over time, respectively. Models to account for tropospheric delay, multipath reflections, and receiver noise are updated as well.

The fourth section of this paper describes how these measurement error models are used in a batch airborne estimator and detector. We define a modular batch ARAIM implementation, which only requires minor modifications to conventional snapshot ARAIM. The inputs to the batch are CSC measurements (same as snapshot), augmented with carrier measurements, and stacked over few, infrequent sample times within the fixed batch interval (e.g., three sample times at 5 min intervals over 10 min). Fault detection is then performed using a batch multiple hypothesis solution separation (MHSS) algorithm. Batch-MHSS is similar to snapshot ARAIM, except that a time-sequence of measurements is processed rather than a single set of CSC data, and that the nominal bias due to signal deformation (specified in [1, 2]) is treated differently. The batch formulation runs sequentially using a sliding-window mechanism. Kalman filter (KF) implementations [15] will be investigated in future work to further reduce computation load.

In the fifth section of this paper, we discuss performance commitments by the ground segment, i.e., by either the constellation service provider (CSP) or by the air navigation service provider (ANSP). In ARAIM, the ground commits to integrity parameters, which are broadcast in the ISM to the aircraft where they serve as basis for integrity risk (or PL) evaluation [1-3]. The integrity parameter set would have to be extended from including URA for snapshot ARAIM to URA-and-URRA for batch ARAIM. URRA specifications are readily described for GPS in [16], but not fully defined yet. Also, the broadcast ISM must be augmented to include information on URRA (only few bits are needed to activate the time-sequential ARAIM module).

The sixth section of this paper analyzes batch ARAIM. A performance assessment is presented for aircraft approach applications using ARAIM with dual-frequency GPS and Galileo satellite measurements. We quantify the impact of SV motion by comparing the integrity performance assuming frozen (i.e., time-invariant) versus unfrozen satellite geometries. Performance sensitivity to URRA and to batch interval length is also evaluated. It suggests that, based on currently-achieved URRA values, only three samples over a ten-minute batch period are needed to efficiently exploit satellite motion. In addition, worldwide availability maps show that batch ARAIM can effectively augment snapshot ARAIM in order to meet LPV-200 requirements even with depleted constellations.

Under conditions described in the paper, batch ARAIM can satisfy much more stringent requirements, including a 10 meter vertical alert limit.

A FIRST ANALYSIS OF THE IMPACT OF GEOMETRIC DIVERSITY ON BIAS ESTIMATION

This work aims at exploiting changes in satellite geometry to obtain fast and accurate estimates of carrier phase cycle ambiguities [4]. Implementations of this principle for aircraft precision approach and landing include the pseudo-satellite ('pseudolite')-based Integrity Beacon Landing System (IBLS) in the early 1990's [17-19], an augmentation of GPS using low earth orbiting (LEO) 'GlobalStar' satellites in 2000 [20], and a GPS augmentation system using Iridium LEO satellites in 2010 [14]. In each of the above references, greatly improved positioning performance was achieved by exploiting the fast relative angular motion between user receiver and the few ranging sources (pseudolites or LEO SVs) in view during short (five-to-ten minute long) mission durations.

In contrast, in this work, we only consider measurements from medium earth orbiting (MEO) GNSS satellites, which are slowly moving from the perspective of a user near the surface of the earth. It is the *multiplicity* of ranging sources from several GNSS constellations that is exploited here to achieve a significant accumulated geometry change.

To reinforce this idea, we analyze an illustrative example of a two-step carrier phase-based aircraft position estimation process represented in Figure 1. This qualitative exercise aims at demonstrating that the accumulated geometric variations form multiple SVs can be a driving mechanism for carrier phase positioning.
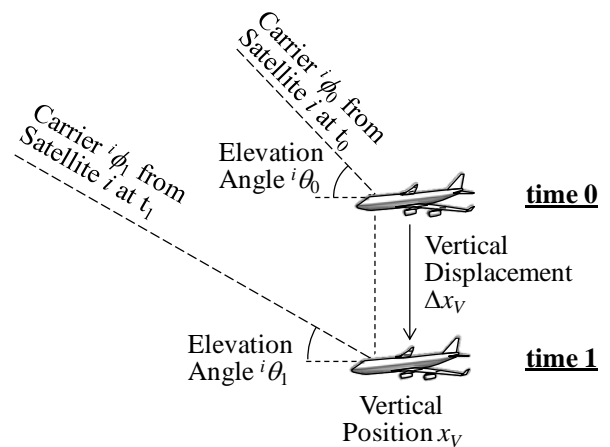

Fig. 1 Aircraft Positioning Example to Illustrate the Impact of SV Motion on Estimation Error Reduction

Let n and n_C respectively be the number of satellites in view and the number of constellations used for navigation. In a first step, carrier phase measurements differenced over times t_0 and t_1 from $n_C + 3$ satellites are used to determine the three dimensional aircraft displacement and the n_C changes in receiver clock biases over the time interval $\Delta t = t_1 - t_0$. The vertical displacement Δx_V estimated using these time-differenced carrier measurements is unambiguous and accurate, but the absolute aircraft position at t_1, noted x_V for the vertical coordinate, is unknown. In a second step, the contribution of the remaining n_* SVs over Δt is exploited, where $n_* = n - 3 - n_C$. Appendix A shows that the resulting estimation error variance on x_V can be expressed as:

$$\sigma_V^2 = \frac{2\sigma_{\phi*}^2}{\displaystyle\sum_{i=1}^{n_*}\left(\sin{}^i\theta_0 - \sin{}^i\theta_1\right)^2} \tag{1}$$

where

$\sigma_{\phi*}^2$ is the variance of the ionosphere-free time-differential carrier measurement, adjusted for Δx_V

${}^i\theta_0$ is the elevation angle for SV i at some initial time t_0

${}^i\theta_1$ is the elevation angle for SV i at a later time t_1

Equation (1) describes two fundamental mechanisms by which σ_V^2 can be reduced. First, if angular variations between ${}^i\theta_0$ and ${}^i\theta_1$ amount to zero for all SVs, then carrier phase signals alone provide no absolute positioning information. But, with SV motion, the larger the angular variation is, the smaller σ_V^2 becomes [21]. Second, the larger the number of visible SVs n_* is, the smaller σ_V^2 becomes. Further results in Appendix A suggest that low-elevation satellite motion contributes more to vertical positioning than high-elevation SV motion does.

In multi-constellation ARAIM, even though ${}^i\theta$-variations may be small over short time periods, the number n_* of contributing terms in the denominator of Equation (1) can be large enough to provide significant σ_V^2 reduction. For a coarse numerical example, if we assume hypothetical values of $n = 12$, $n_C = 2$, ${}^i\theta_0 = 30\deg$ for $i = 1,...,n_*$, $\Delta t = 10\min$, $\sigma_{\phi*}^2 = 5m$ (accounting for the Δx_V-adjustment, receiver noise, multipath, and residual tropospheric errors), and a rate of change in elevation angle ${}^i\dot\theta = 0.005\deg/s$, we find $\sigma_V = 4.7m$. This value of σ_V, obtained even without CSC measurements, can be sufficient to meet a 35 m alert limit. This is because σ_V multiplied by an integrity multiplier of 5.3 (corresponding to a 10^{-7} integrity risk requirement) is 25 m, significantly smaller than 35 m. The remainder of the paper aims at evaluating positioning integrity for more realistic estimation processes, measurement error models, multi-GNSS SV geometries, and integrity requirements.

Both snapshot and batch estimation are represented in Figure 2. Let n be the number of satellites in view, and q the number of samples, collected from filter initiation at time-epoch 0 to current time q. For snapshot estimation, raw code measurements ${}^i\rho_{0,...q}$ for SV i (as indicated by the left superscript) are smoothed using carrier data ${}^i\phi_{0,...q}$ sampled at times 0 to q (right subscripts). Carrier-smoothed code measurements ${}^i\bar\rho_q$ are output by Hatch filters (HF) at time q for satellites $i = 1,...,n$. ARAIM error models specify 'steady-state' CSC standard deviations. HF initiation time 0 is therefore assumed to be far enough in the past to reach steady-state. CSC measurements ${}^i\bar\rho_q$ are then used, for example, in a weighted least squares (WLS) estimator [1] and a MHSS detector [2-3], to determine user position $\hat x_{SNAP}$ and protection levels at one instant in time.

In parallel, the modular design of batch ARAIM is represented in Figure 2. Three additional parameters are introduced. Let T_B be the batch period, i.e., the finite time interval over which measurements are processed: T_B determines the amount of change in SV geometry (e.g., we will use $T_B = 10$ min in the next sections of the paper). Also, let T_S be the sampling interval, i.e., the time between raw samples within the batch (e.g., $T_S = 0.5$ s). Let T_{BS} be the batch sampling interval within the batch period T_B. Because in this modular batch process, noise averaging is performed in separate HF's, T_{BS} can be selected much larger than the raw measurement sampling period T_S ($T_{BS} >> T_S$).

In Figure 2, CSC data $^i\bar{\rho}_q$ are augmented with carrier measurements $^i\phi_q$ and stacked at infrequent batch sample intervals T_{BS} (nominally $T_{BS}=5\,\text{min}$) over the batch interval T_B (nominally $T_B=2T_{BS}=10\,\text{min}$). T_{BS} is selected much larger than the raw measurement sampling period $T_S=0.5\text{s}$ ($T_{BS}>>T_S$). This compact time-sequence of few measurements is processed in a WLS estimator to simultaneously estimate user position $\hat{x}_{BATCH}$ at time q and floating cycle ambiguities, and in an MHSS detector similar to the snapshot algorithm.

This CSC-based batch ARAIM method only requires a minor augmentation of the existing snapshot ARAIM algorithms. It exploits two key estimation principles

- code noise averaging using CSC from HFs — also used in snapshot ARAIM
- SV motion using few carrier measurements — not used in snapshot ARAIM

This modular design is also much more computation and memory efficient than the 'raw batch' in [13], which had to process more than a thousand raw code and carrier signals collected at $T_S=0.5\text{s}$ sampling periods. Preliminary evaluation in [13] suggests that the performance of this new batch implementation (with $T_{BS}=5\,\text{min}$, $T_B=10\,\text{min}$) is only slightly poorer than that of a 'raw batch' (with $T_S=0.5$ s, $T_B=10\,\text{min}$).
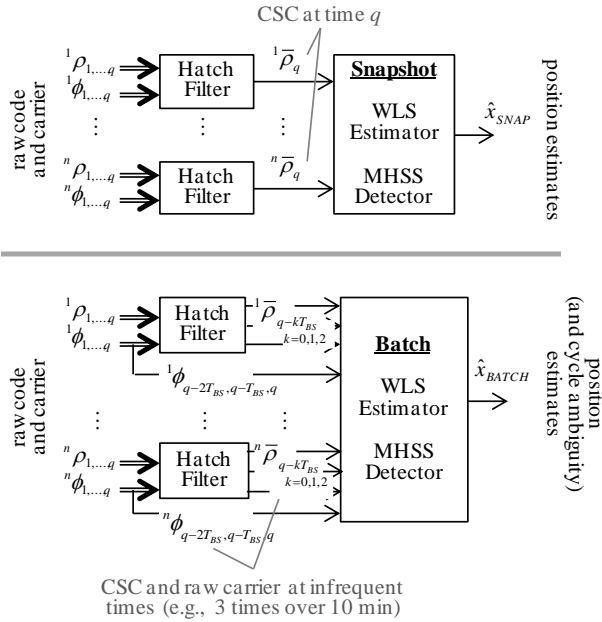

Fig. 2 Overview of 'Snapshot' ARAIM Estimation (top) vs. 'Batch' ARAIM (bottom)

The first key challenge in this work is that the ARAIM measurement error models in [1] were only established for CSC code $^i\bar{\rho}_q$, using large data collection campaigns in [22, 23]. However, evaluating the batch ARAIM performance requires raw measurement error models for $^i\phi_{1,...q}$ and $^i\rho_{1,...q}$. The next section addresses this issue.

DERIVATION OF RAW MEASUREMENT ERROR MODELS OVER TIME

This section aims at deriving statistical error models over time for raw measurements used in batch ARAIM. This work provides refinement and experimental validation of prior research on measurement error time correlation in [13, 14]. It also aims at finding error models that are consistent with the well-established CSC models experimentally validated in [22, 23] and used in ARAIM [1-3].

The linearized ionospheric-error-free code and carrier phase measurement equations for satellite i at time k respectively are:

$$^i\rho_k = -^i\mathbf{e}_k^T\mathbf{x}_k + \tau_k + {}^i\varepsilon_{E,k} + {}^i\varepsilon_{T,k} + {}^i\varepsilon_{MP,\rho,k} + {}^i\varepsilon_{RN,\rho,k} + {}^ib_{\rho,k} \quad (2)$$

$$^i\phi_k = -^i\mathbf{e}_k^T\mathbf{x}_k + \tau_k + {}^i\eta + {}^i\varepsilon_{E,k} + {}^i\varepsilon_{T,k} + {}^i\varepsilon_{MP,\phi,k} + {}^i\varepsilon_{RN,\phi,k} + {}^ib_{\phi,k}$$

where

$^i\mathbf{e}_k$ is the 3×1 line-of-sight vector in a local reference frame (e.g., North-East-Down or NED) for satellite i at time k

$\mathbf{x}_k$ is the 3×1 user position vector in NED

τ_k is the receiver clock offset

$^i\varepsilon_{T,k}$ is the tropospheric error

$^i\varepsilon_{E,k}$ is the SV clock and orbit ephemeris error

$^ib_{\rho,k}$ is a nominal bias on $^i\rho_k$ primarily due to code signal deformation (SD)

$^ib_{\phi,k}$ is a nominal bias on $^i\phi_k$, such that $^ib_{\phi,k} << {}^ib_{\rho,k}$ (carrier is unaffected by SD), included to account for small mean values in the paired overbounding process [24].

$^i\eta$ is the carrier phase cycle ambiguity (constant over time)

$^i\varepsilon_{MP,\rho,k}$ and $^i\varepsilon_{MP,\phi,k}$ respectively are code and carrier errors due to multipath

$^i\varepsilon_{RN,\rho,k}$ and $^i\varepsilon_{RN,\phi,k}$ respectively are code and carrier receiver noise terms

The following subsections describe models for each individual source of error.

Satellite clock and orbit ephemeris error

The satellite clock and orbit ephemeris error equation for satellite i at time k is:

$$^i\varepsilon_{E,k} = {^ib_E} + {^ig_E}\left(t_k - t_q + T_B\right) + {^i\varepsilon_{RES,k}} \qquad (3)$$

where

^ib_E is an unknown, constant bias

^ig_E is an unknown, constant gradient

$t_q - T_B$ is the first time-epoch of the batch interval

t_k represents any time k during the batch interval, such that $1 \le k \le q$, where q is the last epoch of the batch interval

$^i\varepsilon_{RES,k}$ residual errors not captured by the 'bias plus ramp' model

The first term ^ib_E in Equation (3) captures the instantaneous uncertainty in $^i\varepsilon_{E,k}$. It is set according to ARAIM assumptions, i.e., ^ib_E is assumed zero-mean normally distributed with variance σ^2_{URA}. We use the notation: $^ib_E \sim N(0, \ \sigma^2_{URA})$ and we assume: $\sigma_{URA} = 1$ m [2]. This standard deviation represents URA values that are expected to be achievable within the next decade, when GPS satellites older than Block IIF are decommissioned.

It can easily be shown that a time-invariant bias ^ib_E affecting a sequence of raw code measurements input to a Hatch filter causes the same error ^ib_E in the resulting output CSC $^i\bar{\rho}_q$. But, the ARAIM error model does not specify whether nominal SV clock and orbit errors can be assumed constant over any particular time interval. To account for temporal error variations, the second term in Equation (3) is added: it is a ramp over time $(t_k - t_1)$ with an unknown but constant gradient ^ig_E, accounting for linear deviations from the initial value. Reference [14] gives evidence that periodic variations of orbit errors are on the order the MEO GNSS orbital period, which supports the use of a simple linear model over ten minutes. It also cites references [25-27] to establish a distribution on the rate of change of orbit/clock errors: $^ig_E \sim N(0,(4.7 \cdot 10^{-4} \text{ m/s})^2)$.

To further validate Equation (3), an experimental data analysis is carried out, which completes the work in [13].

Similar to prior work in [2, 26, 28], precise GPS satellite orbit and clock estimates from the National Geospatial-Intelligence Agency (NGA) are considered 'truth' reference data, and are compared to broadcast GPS ephemerides archived by the Crustal Dynamics Data Information System (CDDIS). To complement the work in [2, 26, 28] that addressed instantaneous errors, the focus in this work is on the validation of error model characteristics *over time*.

In this analysis, a set of data from January 4, 2015 to September 19, 2015 is processed, for eight Block IIF satellites (PRNs 1, 3, 6, 9, 25, 26, 27, and 30). The bias-plus-ramp model in Equation (3) is fit to truth-minus-broadcast data. Because NGA orbit data is only provided every five minutes, the fit interval is selected to be 30 minutes long. This is larger than the example 10-minute batch period assumed in the next sections of this paper. It will provide conservative results because residual fitting errors are larger over 30 min than they would be over 10 min.

Based on this data, empirical parameter distributions for ^ib_E, ^ig_E and $^i\varepsilon_{RES,k}$ are established. These are then bounded in the cumulative distribution function (CDF)-sense [24, 29] using Gaussian distributions. The standard deviations of the over-bounding Gaussian functions are given in Table 1 for the clock error contribution, and for the three-dimensional orbit errors. Orbit errors are expressed in a local-level, satellite-fixed reference frame, in terms of the in-track, cross-track and radial components [28]. Because GPS satellites are at altitudes of about 20,000 km, user receivers near the surface of the earth are affected by ranging errors that are mostly due to the radial orbit and clock components. Fortunately, orbit radial and clock errors are significantly smaller than orbit in-track and cross-track components, as shown in Table 1.

To get a conservative estimate of the error parameter variance σ^2_{BE} for ^ib_E while taking into account the worst-case geometry between SV and user receiver near earth surface, we use the following equation from [28]:

$$\sigma^2_{BE} = \sigma^2_{BE,CLK} + \sigma^2_{BE,R} + 0.24^2\left(\sigma^2_{BE,I} + \sigma^2_{BE,C}\right) \qquad (4)$$

where 0.24 is a multiplier accounting for the worst-case projection of non-radial orbit error components; $\sigma^2_{BE,CLK}$, $\sigma^2_{BE,R}$, $\sigma^2_{BE,I}$ and $\sigma^2_{BE,C}$, respectively, are the variances of the clock, orbit radial, in-track and cross-track error components contributing to ^ib_E. The same can be done for the variance σ^2_{GE} of ^ig_E. Equation (4) is consistent with equation (A-1) in [16] (although providing a slightly looser bound because different SV elevation mask angles are considered).

Experimental data analysis in Table 1 shows that $\sigma_{BE} = 0.61\,\mathrm{m}$ and $\sigma_{GE} = 1.8 \cdot 10^{-4}\,\mathrm{m/s}$, which are both much smaller than the assumptions mentioned above. In the upcoming availability analysis, we will assume $\sigma_{BE} = \sigma_{URA} = 1\,\mathrm{m}$ and $\sigma_{GE} = \sigma_{URRA} = 4.7 \cdot 10^{-4}\,\mathrm{m/s}$.

In addition, the distribution of residual errors ${}^{i}\varepsilon_{RES,k}$ are plotted for the orbit radial and orbit in-track components in Figs. 3 and 4, respectively. ${}^{i}\varepsilon_{RES,k}$ is obtained by removing the best fit bias-plus-ramp model from the truth-minus-broadcast data. The figures show that ${}^{i}\varepsilon_{RES,k}$ is not negligible as compared to other error sources affecting carrier measurements. As could be expected from prior analyses [2, 26, 28], radial error components are much larger than in-track errors. We cannot determine what parts of these residuals are caused by errors in NGA 'truth' data. We therefore attribute the entire residual errors to SV clock and orbit ephemeris errors, and account for them in the availability analysis, assuming:

$$ {}^{i}\varepsilon_{RES,k} \sim N\!\left(0,\ (0.056\ \mathrm{m})^2\right) \tag{5} $$

where the standard deviation of 0.056 m was obtained using the same formula as in Equation (4) but applied to ${}^{i}\varepsilon_{RES,k}$ (values listed in the rightmost column of Table 1). Future work will include a detailed analysis of the time-characteristics of ${}^{i}\varepsilon_{RES,k}$ which, for now, is modeled as white noise for samples taken at intervals T_{BS}, several minutes apart. (We will assume a $T_{BS} = 5\,\mathrm{min}$ in the sixth section later in this paper.)

As an alternative to Equation (3), Appendix B evaluates a quadratic model for SV clock and orbit ephemeris errors. This quadratic model halves the standard deviation of residual errors ${}^{i}\varepsilon_{RES,k}$ as compared to the linear model. But, it would require additional CSP or ANSP commitments on the User Range Acceleration Accuracy (URAA), and extra parameters in the broadcast ISM. The quadratic model is not employed in this paper, but may be further investigated in future work.

Tropospheric Delay

The troposphere error model is also modified as compared to [13]. The tropospheric delay for SV i at time k is modeled as:

$$ {}^{i}\varepsilon_{T,k} = {}^{i}c_{T,k}\,{}^{i}\varepsilon_{ZID,k} \tag{6} $$

Table 1. Linear Error Model Parameter Over-Bounding Standard Deviations

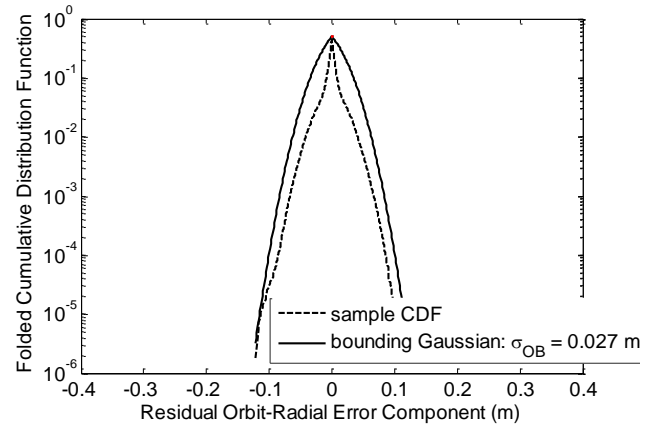|	Standard deviation of bounding Gaussian function		
	for b_E	for g_E	for ε_{RES}
Clock component	0.27 m	$1.0 \cdot 10^{-4}$ m/s	0.042 m
Orbit radial	0.30 m	$1.1 \cdot 10^{-4}$ m/s	0.027 m
Orbit in-track	1.22 m	$3.5 \cdot 10^{-4}$ m/s	0.084 m
Orbit cross-track	1.46 m	$2.4 \cdot 10^{-4}$ m/s	0.072 m
Overall (using (5))	0.61 m	$1.8 \cdot 10^{-4}$ m/s	0.056 m

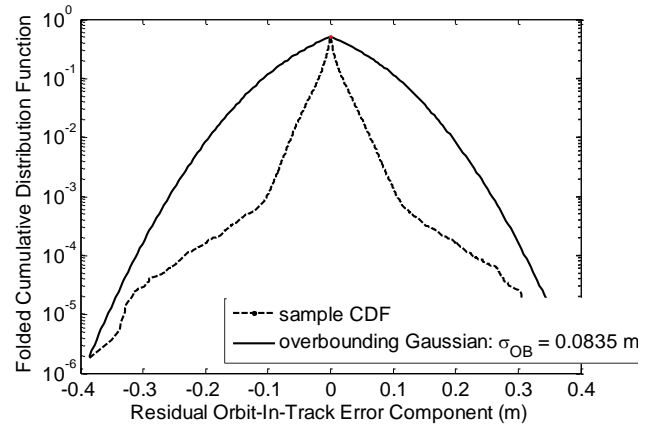**Fig. 3 Folded CDF (Empirical and Bounding Gaussian) for the Orbit-Radial Component of the Residual Error**

Fig. 4 Folded CDF (Empirical and Bounding Gaussian) for the Orbit-In Track Component of the Residual Error

where

$^{i}\varepsilon_{ZID,k}$ is the zenith tropospheric delay for SV i at time k

h_0 is the tropospheric scale height ($h_0 = 7000\,\text{m}$)

h_k is the aircraft height at time k

$^{i}c_{T,k}$ is the tropospheric zenith-to-slant mapping coefficient:

$$^{i}c_{T,k} = 1.001 \Big/ \sqrt{0.002001 + (\sin(^{i}\theta_k))^2}$$

$^{i}\theta_k$ is the elevation angle for SV i at time k

Prior work in [13] modeled the tropospheric delay time-correlation assuming that tropospheric refractivity was unknown, but constant over T_B [30]. In this paper, we no longer make this assumption, the resulting error model is much more conservative. We use:

$$^{i}\varepsilon_{ZID,k} \sim N(0,\ \sigma_{ZID}^2)\ ,\ \ \sigma_{ZTD} = 0.12\,\text{m}\ [1] \qquad (7)$$

Receiver Noise and Multipath Error

We use the receiver noise and multipath error model derived in [13], based on [1, 14, 22-24, 29]. Time-correlated raw code and carrier measurement errors due to multipath reflections are modeled as first order Gauss Markov Processes (GMP) with time constant T_{MP}, with $T_{MP} = 80\,\text{s}$:

$$^{i}\varepsilon_{MP,\rho,k} \sim N(0,\ \sigma_{MP,\rho}^2)\ ,\ \ ^{i}\varepsilon_{MP,\phi,k} \sim N(0,\ \sigma_{MP,\phi}^2)$$

$$^{i}\sigma_{MP,\rho,k} = 1.5\,^{i}\sigma_{MP,\bar{\rho},k}\ ,\ \ ^{i}\sigma_{MP,\phi,k} = 0.015\,^{i}\sigma_{MP,\bar{\rho},k} \quad (8)$$

The ARAIM elevation-dependent model for $\sigma_{MP,\bar{\rho}}^2$ given in [1] for GPS is, in units of meters:

$$^{i}\sigma_{MP,\bar{\rho},k} = c_{IF}\big(0.13 + 0.53\exp(-^{i}\theta_k/10)\big) \qquad (9)$$

where

c_{IF} is the ionosphere-free measurement combination multiplier:
$$c_{IF} = \sqrt{(f_{L1}^4 + f_{L5}^4)/(f_{L1}^2 - f_{L5}^2)^2}$$

f_{L1}, f_{L5} respectively are L1 and L5 frequencies

$^{i}\theta_k$ is the elevation angle in degrees for SV i at time k

Similar, The time-uncorrelated CSC receiver noise standard deviation assumed in ARAIM [1] in units of meters, is given by:

$$^{i}\sigma_{RN,\bar{\rho},k} = c_{IF}\big(0.15 + 0.43\exp(-^{i}\theta_k/6.9)\big) \qquad (10)$$

Raw code and carrier standard deviations are then expressed as [13]:

$$^{i}\sigma_{RN,\rho,k} = 9.8\,^{i}\sigma_{RN,\bar{\rho},k}\ ,\ \ ^{i}\sigma_{RN,\phi,k} = 0.1\,^{i}\sigma_{RN,\bar{\rho},k} \quad (11)$$

The only source of error left unaddressed in Equation (2) is $^{i}b_{SD,k}$, which is dealt with in the next section. It is worth noting that the robustness of the error models can be ensured by selecting a large batch sampling interval T_B. The correlation time constants for multipath error $^{i}\varepsilon_{MP,\rho,k}$ and $^{i}\varepsilon_{MP,\phi,k}$, tropospheric delay $^{i}\varepsilon_{T,k}$, and residual SV clock and orbit ephemeris errors $^{i}\varepsilon_{RES,k}$ can be roughly approximated, as long as they are significantly smaller than T_{BS}. Evidence of this will be established in future work.

AIRBORNE BATCH ESTIMATOR AND DETECTOR DESIGN

In this section, CSC and raw code and carrier measurement error models derived above are incorporated in a batch estimator and in a batch-MHSS RAIM fault-detection algorithm that enables integrity risk evaluation. This batch implementation is formulated in a computationally efficient process illustrated in Figure 2 and referred to as 'batch ARAIM'.

Batch Measurement Equation

For each SV i, CSC and carrier measurements at $p = T_B/T_{BS} + 1$ sample times, from times $q - T_B$ to q in T_{BS} increments, are respectively stacked in $p \times 1$ vectors $^{i}\bar{\rho}$ and $^{i}\varphi$. These vector are then arranged in a $2pn \times 1$ batch measurement vector (n is number of visible SVs):

$$\begin{bmatrix} \varphi^T & \bar{\rho}^T \end{bmatrix}^T = \begin{bmatrix} ^{1}\varphi^T & \cdots & ^{n}\varphi^T & ^{1}\bar{\rho}^T & \cdots & ^{n}\bar{\rho}^T \end{bmatrix}^T \quad (12)$$

This vector can be expressed in terms of state variables, and of measurement error vectors as:

$$\begin{bmatrix} \varphi \\ \bar{\rho} \end{bmatrix} = \begin{bmatrix} \mathbf{G} & \mathbf{H}_N & \mathbf{H}_{ERR} \\ \mathbf{G} & \mathbf{0}_{pn \times n} & \mathbf{H}_{ERR} \end{bmatrix} \begin{bmatrix} \mathbf{u} \\ \boldsymbol{\eta} \\ \mathbf{s}_{ERR} \end{bmatrix} + \begin{bmatrix} \mathbf{v}_{TRNM,\phi} \\ \mathbf{v}_{TRNM,\bar{\rho}} \end{bmatrix} + \begin{bmatrix} \mathbf{b}_\phi \\ \mathbf{b}_{\bar{\rho}} \end{bmatrix} \quad (13)$$

where

    $\mathbf{u}$ is a $5q \times 1$ vector of positions and GPS and Galileo receiver clock offsets at all times (assuming a dual-constellation GNSS)

    $\mathbf{\eta}$ is an $n \times 1$ vector of cycle ambiguities:

    $\mathbf{s}_{ERR}$ is a $2(n+1) \times 1$ vector of constant error states.

    $\mathbf{0}_{a \times b}$ is an $a \times b$ matrix of zeros

Vector $\mathbf{u}$ is constructed using the following equations:

$$\mathbf{u} = \begin{bmatrix} \mathbf{u}_1^T & \cdots & \mathbf{u}_k^T \end{bmatrix}^T \quad , \quad \mathbf{u}_k = \begin{bmatrix} \mathbf{x}_k^T & \tau_{GPS,k} & \tau_{GAL,k} \end{bmatrix}^T \quad (14)$$

where $\mathbf{x}_k$ is the three-dimensional aircraft position vector at time k, $\tau_{GPS,k}$ and $\tau_{GAL,k}$ are the receiver clock offsets for GPS and Galileo respectively, assuming that the time-offset between the two constellations is unknown.

The vector of constant cycle ambiguities is defined as:

$$\mathbf{\eta} = \begin{bmatrix} {}^1\eta & \cdots & {}^n\eta \end{bmatrix}^T \quad (15)$$

The vector of error states is given by:

$$\mathbf{s}_{ERR} = \begin{bmatrix} \mathbf{b}_E^T & \mathbf{g}_E^T \end{bmatrix}^T \quad (16)$$

where $\mathbf{b}_E$ and $\mathbf{g}_E$ are the $n \times 1$ vectors of constant clock and orbit ephemeris biases and gradients for all n satellites constructed following the exact same pattern as $\mathbf{\eta}$ in Equation (15).

Error states $\mathbf{s}_{ERR}$ are included in the state vector, not because their estimated values are of particular interest, but because state augmentation is a practical way to incorporate measurement error dynamics. Prior knowledge on state variables $\mathbf{u}$ is captured in a diagonal state information matrix (inverse of covariance matrix) with diagonal elements:

$$\begin{bmatrix} \mathbf{0}_{1 \times (5p+n)} & \sigma_{BE}^{-2} \mathbf{1}_{1 \times n} & \sigma_{GE}^{-2} \mathbf{1}_{1 \times n} \end{bmatrix}$$

This a-priori knowledge of state estimate errors can directly be incorporated in the estimator by adding up information matrices as described in Section 2.1.2 of [12]. Or, it can be included by measurement vector augmentation, i.e., assuming pseudo-measurements on $\mathbf{s}_{ERR}$ as in [14, 31].

The batch geometry matrix $\mathbf{G}$ and state coefficient matrices $\mathbf{H}_N$ and $\mathbf{H}_{ERR}$ are not explicitly expressed here

to limit the length of the paper. Other batch realizations including error states for different applications can be found in [14, 31].

Vector $[\mathbf{v}_{TRNM,\phi}^T \quad \mathbf{v}_{TRNM,\bar{\rho}}^T]$ accounts for random troposphere, receiver noise, and multipath errors affecting carrier and code signals. Its covariance matrix is noted $\mathbf{V}$. Matrix $\mathbf{V}$ is built as follows. First, for the troposphere contribution, matrix $\mathbf{V}$ is partitioned in four $pn \times pn$ identical blocks made of diagonal matrices capturing the fact that the troposphere identically affects code and carrier. Then, the troposphere covariance is added to that of receiver noise and multipath errors. The multipath and receiver noise covariance contribution is a fully populated matrix that accounts for multipath time-correlation, for HF smoothing time-correlation, and for CSC-to-carrier correlation. A detailed description of how to construct $\mathbf{V}$ is given in [13].

The $pn \times 1$ vector of nominal biases due to code signal deformation $\mathbf{b}_{\bar{\rho}}$ for all SVs at all times is arranged the same way $\bar{\mathbf{\rho}}$ is in Equation (12). Vector $\mathbf{b}_\phi$ is arranged in a similar fashion, but takes much smaller values because carrier phase measurements $\mathbf{\varphi}$ are not affected by signal deformation. (Note that for carrier signals, biases that are constant over the short batch interval will be absorbed into the floating cycle ambiguity states.)

Next we consider the batch measurement Equation (13), with an additive $2pn \times 1$ batch fault vector $\mathbf{f}$, which will have to be detected. The resulting batch observation equation can be rewritten in a standard form as:

$$\mathbf{z} = \mathbf{Hx} + \mathbf{v} + \mathbf{f} \quad (17)$$

where

    $\mathbf{z}$ is the batch measurement vector
    $\mathbf{H}$ is the batch observation matrix,
    $\mathbf{x}$ is the batch state vector
    $\mathbf{v}$ is the batch measurement error vector:
        $\mathbf{v} \sim N([\mathbf{b}_\phi^T \quad \mathbf{b}_{\bar{\rho}}^T]^T, \ \mathbf{V})$

Batch Estimator Design

The batch weighted least-squares (WLS) estimate for the state of interest (e.g., for the vertical position coordinate, which is of primary interest in aircraft approach navigation) at the current time q is defined as:

$$\hat{x}_0 \equiv \mathbf{s}_0^T \mathbf{z} \quad (18)$$

where $\mathbf{s}_0$ is the $2pn \times 1$ vector of batch WLS coefficients. (The same notations, with additional details, are used in

[32]). $\hat{x}_0$ in Equation (18) is obtained using all available measurements, and is also referred to as full-set solution. The full-set estimate error is noted ε_0: $\varepsilon_0 \equiv x - \hat{x}_0$, where x is the true value of the state of interest. ε_0 is such that:

$$\varepsilon_0 \sim N\left(b_0 + \mathbf{s}_0^T \mathbf{f}, \ \sigma_0^2 \equiv \mathbf{s}_0^T \mathbf{V} \mathbf{s}_0\right) \qquad (19)$$

where b_0 is the impact on state estimation of $\mathbf{b}_{\bar{\rho}}$ and $\mathbf{b}_\phi$. The ARAIM error model in [1-2] does not specify whether these biases are constant over time, but it assumes that the elements of $\mathbf{b}_{\bar{\rho}}$ and $\mathbf{b}_\phi$ can all be bounded by a maximum value noted b_{nom}: b_{nom}= 0.75 m in [2]. We further assume that ranging errors due to these biases can be different for all satellites. It follows that b_0 can be bounded by:

$$b_0 \leq \left|\mathbf{s}_0^T \mathbf{A}\right| \mathbf{1}_{2pn\times1} b_{nom} \qquad (20)$$

where $|\ |$ denotes the element-wise absolute value operator, and:

$$\mathbf{A} = \begin{bmatrix} 0.05 \ \mathbf{I}_{pn} & \mathbf{0}_{pn\times pn} \\ \mathbf{0}_{pn\times pn} & \mathbf{I}_{pn} \end{bmatrix} \qquad (21)$$

where a factor of 0.05 is used to capture the fact that carrier measurements are not impacted by signal deformation, but may be impacted by small non-Gaussian but bounded errors.

Batch Detector Design

A multiple-hypothesis solution separation (MHSS) batch RAIM method [1, 2, 14, 15, 32, 33] is adopted for detection of $\mathbf{f}$. Let h be the number of fault hypotheses that need to be monitored against (refer to [32, 33] for details on how to determine h). A set of mutually exclusive, exhaustive hypotheses H_i, for $i = 0, ..., h$, is considered. Under H_i, a number n_i of measurements are simultaneously impacted by the fault. The fault-free subset solution, which excludes these n_i measurements, is written as: $\hat{x}_i \equiv \mathbf{s}_i^T \mathbf{z}$, where $\mathbf{s}_i$ is the $2pn\times1$ vector of the subset solution's batch WLS coefficients with zeros for elements corresponding to the n_i faulted measurements [32, 33]. Under H_i, the estimation error ε_i of $\hat{x}_i$ is such that:

$$\varepsilon_i \sim N\left(b_i, \ \sigma_i^2 \equiv \mathbf{s}_i^T \mathbf{V} \mathbf{s}_i\right) \qquad (22)$$

where $$b_i \leq \left|\mathbf{s}_i^T \mathbf{A}\right| \mathbf{1}_{2pn\times1} b_{nom}. \qquad (23)$$

The batch MHSS test statistics are then defined as:

$$\Delta_i \equiv \hat{x}_0 - \hat{x}_i , \text{ for } i = 1, ..., h , \qquad (24)$$

Δ_i is normally distributed with variance [15, 32, 33]:

$$\sigma_{\Delta i}^2 = \sigma_i^2 - \sigma_0^2 \qquad (25)$$

Integrity and Continuity Risk Evaluation

The integrity risk, or probability of hazardous misleading information P_{HMI}, is evaluated using the following upper-bound [32]:

$$P_{HMI} \leq P\left(\ |\varepsilon_0| > \ell \ | \ H_0\right) P_{H0} \\ + \sum_{i=1}^{h} P\left(\ |\varepsilon_i| + T_i > \ell \ | \ H_i\right) P_{Hi} \qquad (26)$$

where

ℓ is the alert limit (AL) that defines hazardous situations: in [2], the vertical AL is ℓ =35m

P_{Hi} is the prior probability of H_i occurrence

H_0 is the fault-free hypothesis

H_i for $i = 1, ..., h$ are the fault hypotheses corresponding to faults on subset measurement 'i' (including single-satellite, multi-satellite, and constellation faults [2])

Under fault-free hypothesis H_0, the detection threshold T_i is set based on an allocated continuity risk requirement C_{REQ} (specified in [2]) to limit the probability of false alarms. T_i can be defined as:

$$T_i = Q^{-1}\left\{\ C_{REQ}/(2hP_{H0}) \ \right\} \sigma_{\Delta i} \qquad (27)$$

where the function $Q^{-1}\{\}$ is the inverse tail probability distribution of the two-tailed standard normal distribution.

It is worth noting that this batch implementation is compatible with estimator optimization methods [2, 7, 9], which are specifically designed to minimize integrity risk while meeting continuity requirements. These methods will be investigated for batch ARAIM in future work.

GROUND SEGMENT AND INTEGRITY SUPPORT MESSAGE AUGMENTATION TO ENABLE BATCH ARAIM

This section discusses the implications of using batch ARAIM as a modular complement to snapshot ARAIM. Just as the User Range Accuracy (URA) is a primary integrity parameter for snapshot ARAIM [1-3], the User Range Rate Accuracy (URRA) is key to batch ARAIM.

First, the foundational definition of a fault, which in snapshot ARAIM is defined in terms of the URA, must be refined when batch ARAIM is implemented to address URRA. A straightforward modification of [34] gives the following definition:

- A Signal in Space (SIS) fault state is said to exist on satellite i in constellation j when the magnitude of the instantaneous SIS ranging error is greater than $k_{f,i}\sigma_{URA,i,j}$ at the worst user location, *or when the magnitude of the "instantaneous" SIS range rate error over a predefined time period (e.g., 10 min) is greater than* $k_{f,i}\sigma_{URRA,i,j}$ *at the worst user location* .

This fault definition can then be used as in [34] to define prior probabilities of satellite faults $P_{sat,i,j}$ and of constellation faults $P_{const,j}$. The integrity parameters $\sigma_{URA,i,j}$, $P_{sat,i,j}$, and $P_{const,j}$, and the nominal bias bound b_{nom} in Equation (20) are needed at the aircraft to evaluate navigation integrity. The ground segment, i.e., the constellation service provider (CSP) and/or the air navigation service provider (ANSP) provide quantifiable assurance on the validity of these parameters. In batch ARAIM, a fifth parameter needs to be included: the URRA, noted $\sigma_{URRA,i,j}$.

URRA specifications are readily described for GPS in [16], but they are not fully defined yet. ("A future version of this SPS PS may establish a standard" [16].) Reference [16] notes that a 6-sigma upper bound on the SPS SIS instantaneous User Range Rate Error (URRE) is 0.02 m/s over any 3-second interval. This number corresponding to a 0.003 m/s 1-sigma value is an order of magnitude larger than our observations in Table 1. This is because the value is specified over 3-second period, and probably accounts for high-frequency SV clock variations. As such, it is not applicable over our period of interest of 10-15min. Assuming a 0.003 m/s 1-sigma URRA over 10 min yields unrealistically large user range errors (much larger than specified URAs). Thus, for the performance analysis in the next section, we use the URRA value of 0.0004 m/s established in previous sections.

Finally, consistently with the ARAIM architecture defined in [2], the integrity support message (ISM) can be employed as a means to modify the URA and URRA values assumed at the aircraft. This facilitates the integration of newly-deployed constellations and satellites, which are not expected to achieve low URA's in early phases of operation, but can improve as the GNSS matures, and degrade again as it gets older. Integrity parameters are not expected to change frequently, but should stay constant over months. Multiple alternatives are considered to broadcast URRA values, depending on how many data bits can be allocated to this parameter in the ISM:

- URRA values can be broadcast for each individual satellite
- or, URRA values can be broadcast for sets of satellites, for example, a single bounding URRA could be transmitted per satellite Block, or per constellation
- or, a batch ARAIM validity flag could be incorporated in the ISM, indicating that preset, stored URRA are validated by the ground. These preset values could be uploaded monthly as part of the aircraft database.

If these practical issues are overcome, batch ARAIM can achieve substantial reductions in integrity risk as compared to snapshot ARAIM. Examples of such improvements are quantified in the next section.

BATCH ARAIM INTEGRITY AND AVAILABILITY PERFORMANCE ANALYSIS

This section presents an integrity and availability performance analysis of batch ARAIM as compared to snapshot ARAIM. Sensitivity of navigation integrity risk to batch interval length T_B and URRA value is quantified, and global availability maps are given.

Sensitivity Analysis

A method was developed in [13] to analytical establish the conditions of equivalency between snapshot and batch ARAIM. These analytical relationships were used to ensure that raw measurement error models parameters that are not experimentally set were consistent with ARAIM assumptions in [1, 2]. Equivalency was obtained by artificially freezing the simulated satellite geometry, and by adequately selecting T_B [13].

In Figure 5, we freeze and unfreeze the SV geometry to emphasize the impact of exploiting SV motion in batch ARAIM. The figure shows the integrity risk P_{HMI} in Equation (26) evaluated over 24 hours, at an example

Chicago location (25.5 deg N, -80.1 deg E), assuming dual-frequency measurements from GPS and Galileo. The nominal batch interval T_B is 10 min, and the nominal URRA is $\sigma_{URRA} = 0.0004 \text{m/s}$. Other parameter values that are not directly relevant in this subsection and that are kept constant include: $T_{BS} = 300 \ s$, an example integrity risk requirement $I_{REQ} = 0.98 \cdot 10^{-7}$ [2], a continuity risk requirement $C_{REQ} = 3.9 \cdot 10^{-6}$ [2], a vertical alert limit $\ell = 10 \text{ m}$, and prior probabilities of satellite and constellation faults, both noted P_{Hi} in equation (26), respectively are $P_{sat} = 10^{-5}$ and $P_{const} = 10^{-8}$.

Figure 5 shows that for frozen SV geometries, batch ARAIM performs similar to snapshot ARAIM. It is actually slightly better than snapshot ARAIM because the batch interval T_B is significantly longer than the Hatch filter (HF) transient response time, and over T_B, the process gets some observability on the error states $\mathbf{s}_{ERR}$ in Equation (13). P_{HMI} decreases substantially when unfreezing the SV geometry, especially at the P_{HMI} peaks which are a primary cause for unavailability. In the remainder of the paper, we will no longer artificially freeze geometry.

Figure 6 illustrates the sensitivity of P_{HMI} to T_B. It shows that using batch ARAIM with $T_B = 5 \text{min}$ already provides significant P_{HMI}-reduction as compared to snapshot ARAIM. Further reduction is obtained when increasing T_B to 10 min and 15 min. Larger T_B-values are not considered because of the operational constraints on minimum T_B that are mentioned in "Introduction".

In Figure 7, we investigate the sensitivity of P_{HMI} to URRA, for the nominal value $T_B = 10$ min. Just as URA is key in snapshot ARAIM [2], low URRA (labeled σ_{URRA}) values are instrumental in achieving low P_{HMI} in batch ARAIM. When the experimentally-validated nominal URRA ($\sigma_{URRA} = 0.0004 \text{m/s}$) is increased to $\sigma_{URRA} = 0.004 \text{m/s}$, then the benefit of using SV motion in batch ARAIM becomes negligible, and the corresponding P_{HMI}-curve with diamond markers in Fig. 7 matched that of batch ARAIM for the frozen geometry case in Fig. 5.

Availability Maps

This sub-section evaluates the global availability of LPV-200 navigation requirements to support localizer precision vertical aircraft approach operations down to 200 feet above the ground, using ARAIM with dual-frequency measurements from GPS and Galileo. Nominal simulation parameters are defined in [2], and include:

- a five degree satellite elevation mask
- ARAIM CSC measurement error model parameters in equations (1) to (10), and (21)
- navigation requirements: $I_{REQ} = 0.98 \cdot 10^{-7}$, $C_{REQ} = 3.9 \cdot 10^{-6}$, $\ell = 35$ m
- prior probabilities of faults: $P_{sat} = 10^{-5}$, $P_{const} = 10^{-4}$
- reduced-batch period and sampling interval: $T_B = 10$ min, $T_{BS} = 5$ min
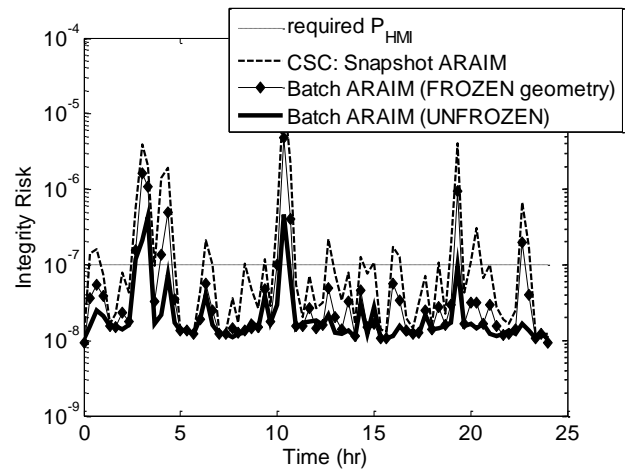- nominal constellations, comprising 24 GPS satellites and 24 Galileo SVs [35]

Fig. 5 Integrity Risk Bound Obtained Using Snapshot Vs. Batch ARAIM: all parameters identical to Fig. 8 (T_B = 600s, T_{RB} = 300s).
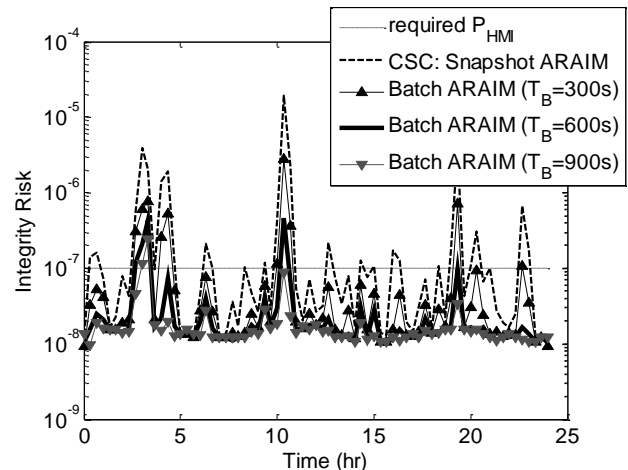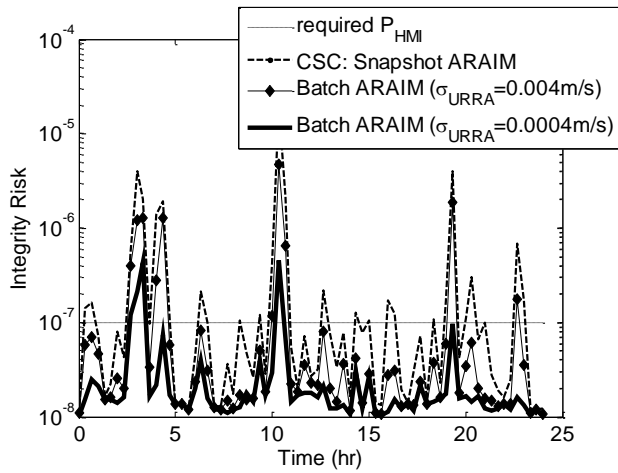

Fig. 6 Integrity Risk Bound Obtained Using Snapshot Vs. Batch ARAIM: all parameters identical to Fig. 8 (T_B = 600s, T_{RB} = 300s).

Fig. 7 Integrity Risk Bound Obtained Using Snapshot Vs. Batch ARAIM: all parameters identical to Fig. 8 (T_B = 600s, T_{RB} = 300s).

Fig. 9 Availability Map for Batch ARAIM using depleted constellations, P_{const} = 10^{-4}, ℓ = 35 m (coverage of 99.5% availability is 90.0%).

These parameters are modified below to evaluate performance sensitivity. In order to account for potential satellite outages, depleted constellations of '24-1' GPS satellites and '24-1' Galileo SVs [35] are considered as well. Additional requirements, including Effective Monitor Threshold (EMT) and fault-free accuracy requirements [2], are included in the simulation but not discussed in this paper as they only have a minor impact on overall availability.

Figures 8 and 9 display availability maps for a 10 deg × 10 deg latitude-longitude grid of locations, for depleted '24-1' GPS and '24-1' Galileo constellations, for satellite geometries simulated at regular 5 minute intervals over a 24 hour period. Availability is computed at each location as the fraction of time where the P_{HMI}-bound meets I_{REQ}.
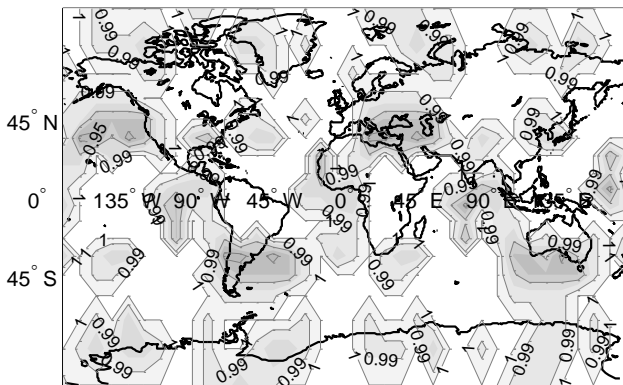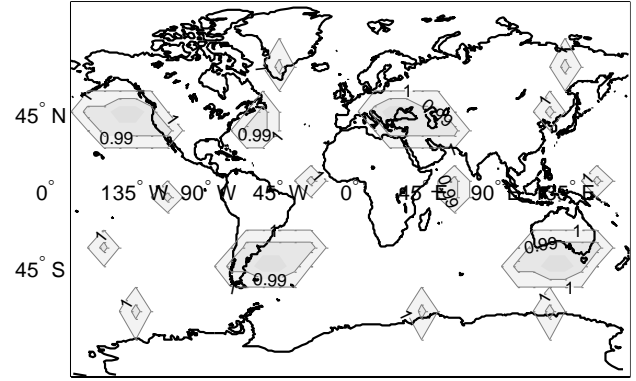
In the figures, availability is color-coded: white color corresponds to a value of 100%, black represents 80%. Constant availability contours are also displayed. The gray areas in Fig. 8 indicate that snapshot ARAIM is clearly outperformed by batch ARAIM in Fig. 9.

The worldwide availability metric given in the figure captions is the weighted coverage of 99.5% availability: coverage is defined as the percentage of grid point locations exceeding 99.5% availability. The coverage computation is weighted at each location by the cosine of the location's latitude, because grid point locations near the equator represent larger areas than near the poles. Figures 8 and 9 show that the coverage of 99.5% availability increases from 62.5 % for snapshot ARAIM, to 90.0% for batch ARAIM, assuming ℓ = 35 m.

This result was obtained using the 'baseline' snapshot ARAIM algorithm described in [1-3]. Reference [2] also provides an 'optimized' estimator, which, when evaluated under the same assumptions as in Fig. 8, provides coverage of 99.5% availability of 81%. Therefore, even using an optimized estimator, coverage using snapshot ARAIM is 9% lower than using batch ARAIM. Furthermore, the optimal estimator approach [2, 7, 9] is compatible with batch ARAIM, so that availability in Fig. 9 can be further improved. This will be investigated in future work.

Figures 10 and 11 evaluate the potential of batch ARAIM to meet requirements that are more stringent than LPV200, including a tight alert limit: ℓ = 10 m. In this case, one key assumption to achieve high availability is that the prior probability of constellation-wide faults must be reduced to $P_{const} = 10^{-8}$. This assumption, also considered in ARAIM (for 'horizontal ARAIM or H-ARAIM in [2]), may be accomplished using the

Fig. 8 Availability Map for Snapshot ARAIM using depleted constellations, P_{const} = 10^{-4}, ℓ = 35 m (coverage of 99.5% availability is 62.5%).

guidelines in [36]. These guidelines exploit additional information from the ANSP ground segment. In Figs. 10 and 11, availability maps assume nominal 24-satellite GPS and Galileo constellations. The same color code as in Figs. 8 and 9 is used. Again, batch ARAIM in Fig. 11 provides a dramatic improvement as compared to snapshot ARAIM in Fig. 10.

Worldwide coverage of 99.5% availability, and of 95% availability (given in parentheses), for the above configurations, for nominal and depleted constellations, are listed in Table 2. Table 2 quantifies the global performance improvement brought by batch ARAIM as compared to snapshot ARAIM. As mentioned throughout the paper, this improvement comes at the cost of higher computation and memory loads, of additional ground segment commitments on URRA, and of few extra parameters in the ISM. It must also be noted that, for aircraft navigation standards that are more stringent than LPV200, and that include ℓ = 10 m, additional requirements are typically involved, e.g., on the communication link between ANSP ground segment and aircraft. Such considerations are beyond the scope of this paper.

Table 2 suggests that a 10 meter alert limit may be reachable using nominal constellations, but for now, only with low coverage. The coverage metric can be deceiving (e.g., availability averaged over all locations in Fig. 11 is 98%). Still, additional research is needed to improve coverage, for example using optimized estimators.

CONCLUSION

In this paper, a new ARAIM integrity monitoring method was devised, which exploits the motion of satellites from multiple GNSS. Raw measurement error models over time were established. These models were then incorporated in batch-type estimation and solution-separation fault-detection processes.

The impact of satellite motion on 'batch ARAIM' was analyzed as a functions of batch period, and then quantified globally in comparison with conventional 'snapshot ARAIM'. The proposed batch ARAIM implementation is slightly more computation and memory expensive than snapshot ARAIM. But, it can provide significant performance improvements both when aiming to achieve LPV200 requirements using depleted constellations, and when trying to meet a much more stringent ten-meter alert limit.

The next step of this research is to investigate ways to further improve availability when trying to achieve 10-meter alert limits, for example by employing non-least-squares estimators specifically designed to minimize integrity risk.
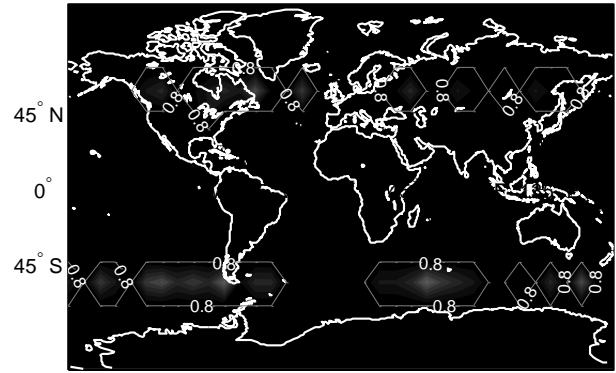

Fig. 10 Availability Map for Snapshot ARAIM using nominal constellations, P_{const} =10^{-8}, ℓ =10 m, (coverage of 99.5% availability is 0%).
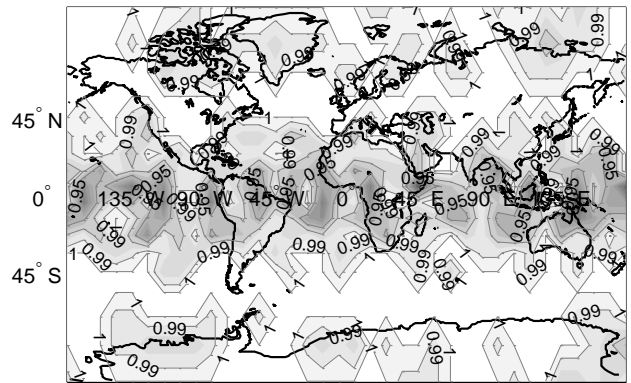

Fig. 11 Availability Map for Batch ARAIM, using nominal constellations, P_{const} =10^{-8}, ℓ =10 m, T_B =900s, (coverage of 99.5% availability is 43%).

Table 2. Coverage of 99.5% Availability, and Coverage of 95% Availability (in parentheses)

	Snapshot ARAIM	Batch ARAIM
nominal constellations , $P_{const} = 10^{-4}$, ℓ =35 m, T_B=600s	94% (100%)	100% (100%)
depleted constellations, $P_{const} = 10^{-4}$, ℓ =35 m, T_B =600s	63% (98%)	90% (100%)
nominal constellations, $P_{const} = 10^{-8}$, ℓ =10 m, T_B =900s	0% (0%)	43% (86%)

ACKNOWLEDGMENTS

However, the opinions in this paper are our own and do not necessarily represent those of any other person or organization.

APPENDIX A: IMPACT OF SV MOTION ON POSITIONING ERROR VARIANCE DERIVATION

The analysis described in this appendix and illustrated in Figure 1 is an extension of the 'Static Surveying' problem given in [21]. In this case, the measurement vectors $\boldsymbol{\varphi}_0$ and $\boldsymbol{\varphi}_1$ include differential carrier phase signals (at times 0 and 1) from satellites i, for $i = 1,...,n$. Simplifying the problem to be one-dimensional along the vertical direction in a local reference frame at the aircraft location, $\boldsymbol{\varphi}_0$ and $\boldsymbol{\varphi}_1$ are written by:

$$\boldsymbol{\varphi}_0 = \mathbf{g}_0 x_V + \boldsymbol{\eta} + \mathbf{v}_0$$
$$\boldsymbol{\varphi}_1 = \mathbf{g}_1 (x_V + \Delta x_V) + \boldsymbol{\eta} + \mathbf{v}_1$$

We define:

$$\boldsymbol{\varphi}_{1*} = \boldsymbol{\varphi}_1 - \mathbf{g}_1 \Delta x_V = \mathbf{g}_1 x_V + \boldsymbol{\eta}_V + \mathbf{v}_{1*}$$

These measurements are expressed in matrix form as:

$$\begin{bmatrix} \boldsymbol{\varphi}_0 \\ \boldsymbol{\varphi}_{1*} \end{bmatrix} = \begin{bmatrix} \mathbf{g}_0 & \mathbf{I}_n \\ \mathbf{g}_1 & \mathbf{I}_n \end{bmatrix} \begin{bmatrix} x_V \\ \boldsymbol{\eta} \end{bmatrix} + \begin{bmatrix} \mathbf{v}_0 \\ \mathbf{v}_{1*} \end{bmatrix}$$

where

$$\boldsymbol{\varphi}_0 = \begin{bmatrix} {}^1\phi_0 & \cdots & {}^n\phi_0 \end{bmatrix}^T, \quad \boldsymbol{\varphi}_{1*} = \begin{bmatrix} {}^1\phi_{1*} & \cdots & {}^n\phi_{1*} \end{bmatrix}^T$$

$$\boldsymbol{\eta} = \begin{bmatrix} {}^1\eta \\ \vdots \\ {}^n\eta \end{bmatrix}, \quad \mathbf{g}_0 = \begin{bmatrix} \sin {}^1\theta_0 \\ \vdots \\ \sin {}^n\theta_0 \end{bmatrix}, \quad \mathbf{g}_1 = \begin{bmatrix} \sin {}^1\theta_1 \\ \vdots \\ \sin {}^n\theta_1 \end{bmatrix}$$

and

x_V is the vertical position to be estimated (displayed in Figure 1)

$\mathbf{I}_n$ is an $n \times n$ identity matrix

${}^i\eta$ carrier phase cycle ambiguity for SV i

The carrier phase measurement noise vector $[\mathbf{v}_{0*}^T \quad \mathbf{v}_{1*}^T]^T$ is assumed zero-mean normally distributed with covariance matrix $\mathbf{I}_{2n}\sigma_{\phi*}^2$. The WLS estimate error variance for Δx_V is given by:

$$\sigma_V^2 = \sigma_{\phi*}^2 \begin{bmatrix} 1 & \mathbf{0}_{1 \times n} \end{bmatrix} \left(\begin{bmatrix} \mathbf{g}_0^T & \mathbf{g}_1^T \\ \mathbf{I}_n & \mathbf{I}_n \end{bmatrix} \begin{bmatrix} \mathbf{g}_0 & \mathbf{I}_n \\ \mathbf{g}_1 & \mathbf{I}_n \end{bmatrix} \right)^{-1} \begin{bmatrix} 1 \\ \mathbf{0}_{n \times 1} \end{bmatrix} \quad (A.2)$$

where

$\mathbf{0}_{a \times b}$ is an $a \times b$ matrix of zeros

Using a popular matrix inversion formula, σ_V^2 becomes:

$$\sigma_V^2 = \frac{2\sigma_{\Delta\phi}^2}{2\mathbf{g}_0^T \mathbf{g}_0 + 2\mathbf{g}_1^T \mathbf{g}_1 - (\mathbf{g}_0^T + \mathbf{g}_1^T)(\mathbf{g}_0 + \mathbf{g}_1)} \quad (A.3)$$

which, using the above definitions of $\mathbf{g}_0$ and $\mathbf{g}_1$ can be written as:

$$\sigma_V^2 = \frac{2\sigma_{\Delta\phi}^2}{\sum_{i=1}^{n} \left(\sin {}^i\theta_0 - \sin {}^i\theta_1 \right)^2} \quad (A.4)$$

This result is commented upon in Section 'A First Analysis of the impact of Geometric Diversity on Bias Estimation'.

Equation (A.4) can be further analyzed considering small angular variations over an infinitesimally small time interval δt. Because in this illustrative example, σ_V^2 becomes infinitely large when ${}^i\theta_0 = {}^i\theta_1$, let us assume that we have prior knowledge on Δx_V with variance $\sigma_{V,prior}^2$. The reasoning is pursued in the information form because information (inverse of variance) can directly be added up. We are interested in determining the contribution $\delta {}^i\sigma_V^{-2}$ of the motion of SV i over δt (other SVs are assumed static) to the a-posteriori Δx_V-estimate information $\sigma_{V,post}^{-2}$: $\sigma_{V,post}^{-2} = \sigma_{V,prior}^{-2} + \delta {}^i\sigma_V^{-2}$. The information $\delta {}^i\sigma_V^{-2}$ can be written as:

$$\delta {}^i\sigma_V^{-2} = \frac{\sigma_{\Delta\phi}^{-2}}{2} \left(\sin {}^i\theta_0 - \sin({}^i\theta_0 + \delta\theta) \right) \quad (A.5)$$

Using a first order Taylor series approximation for small angular variations about θ_0 of the second term in the sum, Equation (A.5) becomes:

$$\delta {}^i\sigma_V^{-2} = \frac{\sigma_{\Delta\phi}^{-2}}{2} \left(\cos({}^i\theta_0) \; \dot{\theta} \; \delta t \right) \quad (A.6)$$

$$\sigma_V^{-2} = \sum_{i=1}^{n-3-n_C} \frac{\sigma_{\phi,V*}^{-2}}{2} \left(\cos(\,^i\theta_0\,) \ \dot{\theta} \ \delta t \right)$$

Low elevation satellites have a zenith angle $^i\theta_0$ approaching $90°$. Equation (A.6) shows that the information contribution $\delta\,^i\sigma_V^{-2}$ is larger for these satellites than for high elevation SVs, both because of the $\sin\,^i\theta_0$ -term, and because $\dot{\theta}$ is larger at low elevations.

APPENDIX B: QUADRATIC ERROR MODEL

The satellite clock and orbit ephemeris error equation for satellite i at time k is:

$$^i\varepsilon_{E,k} = \,^ib_E + \,^ig_E\left(t_k - t_q + T_B\right) + \,^iq_E\left(t_k - t_q + T_B\right)^2 + \,^i\varepsilon_{RES,k}$$

where

^iq_E is an unknown, constant quadratic coefficient

This quadratic error model is processed using nine months of truth-broadcast data processed as described in Section "Derivation of Raw Measurement Error Models Over Time". The resulting overbounding Gaussian standard deviations are listed in Table 3. The residual error deviation in the rightmost column is reduced from 5.7 cm for the linear model (see Table 1) to 3.1 cm for the quadratic model. But, as mentioned in the text, implementing the quadratic error model would require additional commitments on URAA, and extra parameters broadcast in the ISM.

Table 3. Quadratic Error Model Parameter Over-Bounding Standard Deviations

	Standard deviation of bounding Gaussian function			
	for b_E	for g_E	for q_E	for ε_{RES}
CLK	0.27 m	$1.5 \cdot 10^{-4}$ m/s	$5.6 \cdot 10^{-8}$ m/s^2	0.024 m
R	0.30 m	$2.3 \cdot 10^{-4}$ m/s	$9.5 \cdot 10^{-8}$ m/s^2	0.002 m
I	1.42 m	$5.4 \cdot 10^{-4}$ m/s	$2.1 \cdot 10^{-7}$ m/s^2	0.061 m
C	1.22 m	$3.0 \cdot 10^{-4}$ m/s	$1.4 \cdot 10^{-7}$ m/s^2	0.053 m
O	0.6 m	$3.1 \cdot 10^{-4}$ m/s	$1.3 \cdot 10^{-7}$ m/s^2	0.031 m

CLK : clock component; R : orbit radial; I : in-track; C : cross-track
O: overall value (using Equation (5))

REFERENCES

[1] Working Group C. "ARAIM Technical Subgroup. Interim Report Issue 1.0." Technical report, EU-US Cooperation on Satellite Navigation, 2012.

[2] Working Group C. "ARAIM Technical Subgroup. Milestone 2.0 Report." Technical report, EU-US Cooperation on Satellite Navigation, 2014.

[3] Blanch, J., T. Walter, P. Enge, S. Wallner, F. A. Fernandez, R. Dellago, R. Ioannides, I. F. Hernandez, B. Belabbas, A. Spletter, M. Rippl, "Critical Elements for a Multi-Constellation Advanced RAIM," *NAVIGATION*, Vol. 60, No. 1, 2013, pp. 53-69.

[4] Remondi, B., "Pseudo-Kinematic GPS Results Using the Ambiguity Function Method," *Proceedings of the 46th Annual Meeting of the Institute of Navigation*. Atlantic City, NJ. 41-49, NJ, 1990.

[5] Lee, Y. C., "Analysis of Range and Position Comparison Methods as a Means to Provide GPS Integrity in the User Receiver," *Proc. of the 42nd Annual Meeting of The Institute of Navigation*, Seattle, WA, 1986, pp. 1-4.

[6] Parkinson, B. W., and Axelrad, P., "Autonomous GPS Integrity Monitoring Using the Pseudorange Residual," *NAVIGATION*, Vol. 35, No. 2, 1988, pp. 225-274.

[7] Blanch, J., Walter, T., and Enge, P., "Optimal Positioning for Advanced RAIM." *NAVIGATION, Journal of The Institute of Navigation*, Vol. 60, No. 4, 2013, pp. 279-289.

[8] Blanch, J., Walter, T., Enge, P., "Results on the Optimal Detection Statistic for Integrity Monitoring," *Proceedings of the 2013 International Technical Meeting of The Institute of Navigation*, San Diego, California, January 2013, pp. 262-273.

[9] Joerger, M., Langel, S., and Pervan, B., "Integrity Risk Minimization in RAIM - Part 2 - Optimal Estimator Design," submitted to *Journal of Navigation of the Royal Institute of Navigation*, 2014.

[10] Joerger, M., Langel, S., and Pervan, B., "Integrity Risk Minimization in RAIM - Part 1 - Optimal Detector Design." submitted to *Journal of Navigation of the Royal Institute of Navigation*, 2014.

[11] Radio Technical Commission for Aeronautics (RTCA) Special Committee 159. "Minimum Aviation System Performance Standards for the Local Area Augmentation System (LAAS)." Document RTCA/DO-245, 2004.

[12] Crassidis, J., and Junkins, J., *Optimal Estimation of Dynamic Systems*, Chapman & Hall/CRC, Boca Raton, FL, 2004, pp. 123-174.

[13] Joerger, M., and Pervan, B., "Multi-Constellation ARAIM Exploiting Satellite Geometry Change,"

Proceedings of the 28th International Technical Meeting of The Satellite Division of the Institute of Navigation (ION GNSS+ 2015), Tampa, Florida, September 2015, pp. 2688-2704.

[14] Joerger, M., Gratton, L., Pervan, B., and Cohen, C. E., "Analysis of Iridium-Augmented GPS for Floating Carrier Phase Positioning," *NAVIGATION, Journal of The Institute of Navigation*, Vol. 57, No. 2, 2010, pp. 137–160.

[15] Brenner, M., "lntegrated GPS/lnertial Fault Detection Availability," *Proceedings of the 8th International Technical Meeting of the Satellite Division of The Institute of Navigation (ION GPS 1995)*, Palm Springs, CA, 1995, pp. 1949-1958.

[16] U.S. Department of Defense, "Global Positioning System Standard Positioning Service Performance Standard (4th Edition)," September 2008.

[17] Pervan, B., "Navigation Integrity for Aircraft Precision Landing Using the Global Positioning System," PhD Thesis, Stanford University, Stanford, CA, 1996.

[18] Cohen, C., Cobb, S., Lawrence, D., Pervan, B., Powell, D., Parkinson, B., Aubrey, G., Loewe, W. , Ormiston, D., MCNally, D., Kaufmann, D., Wullschleger, V., and Swider, R., "Autolanding a 737 Using GPS Integrity Beacons," *NAVIGATION: Journal of the Institute of Navigation*, Vol 42, No. 3, 1995, pp. 467-486.

[19] Gutt, G., Fischer, S., Sheen, J., and Lawrence, D., "Precision Autoland Guidance of the X-31 Aircraft Using IBLS – The Integrity Beacon Landing System," *AIAA Guidance, Navigation, and Control Conference*, Providence, RI, 2004.

[20] Rabinowitz, M., Parkinson, B., Cohen, C., O'Connor, M., Lawrence, D., "A System Using LEO Telecommunication Satellites for Rapid Acquisition of Integer Cycle Ambiguities," *Proceedings of ION/IEEE Position Location and Navigation Symposium*, Palm Springs, CA, 1998.

[21] Hwang, P. Y. C., "Kinematic GPS for Differential Positioning: Resolving Integer Ambiguities on the Fly," *NAVIGATION*, Vol. 38, No. 1, 1991, pp. 1-16.

[22] Murphy, T., Harris, M., Geren, P., Pankaskie, T., Clark, B., and Burns, J., "More Results from the Investigation of Airborne Multipath Errors," *Proceedings of the 18th International Technical Meeting of the Satellite Division of The Institute of Navigation (ION GNSS 2005)*, Long Beach, CA, September 2005, pp. 2670-2687.

[23] Murphy, T., Harris, M., Beauchamp, S., "Implications of 30-Second Smoothing for GBAS Approach Service Type D," *Proceedings of the 2010 International Technical Meeting of The Institute of Navigation*, San Diego, CA, January 2010, pp. 376-385.

[24] Rife, J. Pullen, S., Enge, P., and Pervan, B., "Paired Overbounding for Nonideal LAAS and WAAS Error Distributions," *IEEE Transactions on Aerospace and Electronic Systems*, Vol. 42, No. 4, 2006, pp. 1386-1395.

[25] Parkinson, B., and Spilker, J., 1996, *Global Positioning System: Theory and Applications Volume 1*, AIAA Progress in Aeronautics and Astronautics, Washington, DC, Volume 163.

[26] Warren, D., Raquet, J., "Broadcast vs. Precise GPS Ephemerides: a Historical Perspective," *GPS Solutions*, Vol. 7, 2003, pp. 151-156.

[27] Gratton, L., "Orbit Ephemeris Monitors for Category I Local Area Augmentation of GPS," MS Thesis, Illinois Institute of Technology, Chicago, IL, 2003.

[28] Cohenour, C., and van Graas, F., "GPS Orbit and Clock Error Distributions", *NAVIGATION, Journal of The Institute of Navigation*, Vol. 58, No. 1, Spring 2011, pp. 17-28.

[29] DeCleene, B, "Defining Pseudorange Integrity - Overbounding," *Proceedings of the 13th International Technical Meeting of the Satellite Division of The Institute of Navigation (ION GPS 2000)*, Salt Lake City, UT, September 2000, pp. 1916-1924.

[30] McGraw, G., Murphy, T., Brenner, M., Pullen, S., and Van Dierendonck, A., "Development of the LAAS Accuracy Models," *Proceedings of the Institute of Navigation GPS Conference*. Salt Lake City, UT, 2000, pp. 1212-1223.

[31] Joerger, M., "Carrier Phase GPS Augmentation Using Laser Scanners and Using Low Earth Orbiting Satellites." Ph.D. Dissertation, Illinois Institute of Technology, 2009.

[32] Joerger, M., Chan, F.-C., Pervan, B., "Solution Separation Versus Residual-Based RAIM", *NAVIGATION, Journal of The Institute of Navigation*, Vol. 61, No. 4, Winter 2014, pp. 273-291.

[33] Blanch, J., Ene, A., Walter, T., and Enge, P., "An Optimized Multiple Hypothesis RAIM Algorithm for Vertical Guidance," *Proceedings of the 20th International Technical Meeting of the Satellite Division of The Institute of Navigation (ION GNSS 2007)*, Fort Worth, TX, September 2007, pp. 2924-2933.

[34] Walter, T., Blanch, J., Joerger, M., Pervan, B., "Determination of Fault Probabilities for ARAIM," *Proceedings of IEEE/ION PLANS 2016*, Savannah, GA, April 2016, pp. 451-461.

[35] almanac files provided by Stanford University, available online at *http://waas.stanford.edu/staff/maast/maast.html*

[36] Walter, T., Blanch, J., "Airborne Mitigation of Constellation Wide Faults," *Proceedings of the 2015 International Technical Meeting of The Institute of Navigation*, Dana Point, California, January 2015, pp. 676-686.